Clim Dyn (2012) 38:1675–1693
DOI 10.1007/s00382-011-1131-0

# Simulation of direct radiative forcing of aerosols and their effects on East Asian climate using an interactive AGCM-aerosol coupled system

**Hua Zhang · Zhili Wang · Zaizhi Wang · Qianxia Liu · Sunling Gong · Xiaoye Zhang · Zhongping Shen · Peng Lu · Xiaodong Wei · Huizheng Che · Laurent Li**

Received: 23 November 2010 / Accepted: 20 June 2011 / Published online: 9 July 2011


**Abstract** An interactive system coupling the Beijing Climate Center atmospheric general circulation model (BCC_AGCM2.0.1) and the Canadian Aerosol Module (CAM) with updated aerosol emission sources was developed to investigate the global distributions of optical properties and direct radiative forcing (DRF) of typical aerosols and their impacts on East Asian climate. The simulated total aerosol optical depth (AOD), single scattering albedo, and asymmetry parameter were generally consistent with the ground-based measurements. Under all-sky conditions, the simulated global annual mean DRF at the top of the atmosphere was $-2.03$ W m$^{-2}$ for all aerosols including sulfate, organic carbon (OC), black carbon (BC), dust, and sea salt; the global annual mean DRF was $-0.23$ W m$^{-2}$ for sulfate, BC, and OC aerosols. The sulfate, BC, and OC aerosols led to decreases of 0.58° and 0.14 mm day$^{-1}$ in the JJA means of surface temperature and precipitation rate in East Asia. The differences of land-sea surface temperature and surface pressure were reduced in East Asian monsoon region due to these aerosols, thus leading to the weakening of East Asian summer monsoon. Atmospheric dynamic and thermodynamic were affected due to the three types of aerosol, and the southward motion between 15°N and 30°N in lower troposphere was increased, which slowed down the northward transport of moist air carried by the East Asian summer monsoon, and moreover decreased the summer monsoon precipitation in south and east China.

**Keywords** AGCM · Aerosol · Radiative forcing · Climate effects · East Asian monsoon

H. Zhang (✉)
Laboratory for Climate Studies, National Climate Center, China Meteorological Administration, 46 Zhongguancun Nandajie, Beijing 100081, China
e-mail: huazhang@cma.gov.cn

Z. Wang
Chinese Academy of Meteorological Sciences, Beijing 100081, China

Z. Wang
National Climate Center, China Meteorological Administration, Beijing 100081, China

Q. Liu · P. Lu · X. Wei
National Climate Center, China Meteorological Administration, 46 Zhongguancun Nandajie, Beijing 100081, China

S. Gong
Air Quality Research Branch, Meteorological Service of Canada, Toronto, ON, Canada

X. Zhang · H. Che
Center for Atmosphere Watch and Services, Chinese Academy of Meteorological Sciences, China Meteorological Administration, Beijing, China

Z. Shen
Shanghai Climate Center, Shanghai, China

L. Li
Laboratoire de Météorologie Dynamique, CNRS/UPMC, Paris, France

## 1 Introduction

Both natural processes and anthropogenic activities contribute to global climate changes. The latter has played an important role in the significant changes in atmospheric components since the beginning of industrialization. Currently, the aerosol climate effects (especially the interactions among aerosols, radiation, and clouds) remain one of the largest uncertainties in model simulation and climate

change assessment (IPCC 2007). Aerosols can affect climate in several ways. Firstly, aerosol particles can directly scatter or absorb infrared and solar radiation, thereby disturbing the energy budget of the earth-atmosphere system (Houghton et al. 1996; Haywood and Ramaswamy 1998). Secondly, aerosol particles acting as cloud condensation or ice nuclei can change cloud microphysical and radiative properties and cloud lifetimes, and hence indirectly affect the climate (Twomey 1977; Albrecht 1989; Ramaswamy et al. 2001; Lohmann and Feichter 2005; IPCC 2007). Thirdly, the absorbing aerosol particles located in cloud layers can strengthen evaporation processes in clouds and thus decrease cloud cover through strongly absorbing solar radiation and heating the atmosphere. This is referred to as the semi-direct effect of aerosols (Hansen et al. 1997; Ackerman et al. 2000). Additionally, absorbing aerosols can be transported over long distances by atmospheric circulation and be deposited onto remote snow/ice surfaces where they may reduce the snow/ice surface albedo and hence increase melting (Warren and Wiscombe 1980; Hansen and Nazarenko 2004; Jacobson 2004; Flanner et al. 2007).

Atmospheric aerosols include sulfate, black carbon (BC), organic carbon (OC), and nitrate, which are mostly produced by human activities, and sea salt and soil dust, which mostly emit naturally. There are five dominant source regions of anthropogenic aerosols: East and South Asia, Western Europe, eastern U.S., South America, and central Africa (Streets et al. 2003; IPCC 2007). The sources of soil dust aerosol mainly locate in deserts and semi-desert regions, such as the Sahara in Africa and deserts of Central and West Asia. Anthropogenic dust sources have been increasing since industrialization because of desertification in some areas (Zhang et al. 2008). Sea salt aerosols are mostly distributed over oceans. Some field studies, such as the Cloud Indirect Forcing Experiment (CIFEX; Wilcox et al. 2006), the Aerosols over China and their Climate Effect (Zhang 2007), the East Asian Regional Experiment (EAREX; Nakajima et al. 2007), have investigated aerosol properties and radiative effects. Satellite data have also been used to estimate the global direct radiative forcing (DRF) of aerosols. Using the latest version of MODIS products, Bellouin et al. (2008) estimated the global annual mean DRF at the TOA with respect to present-day natural aerosols was $-1.30$ and $-0.65$ W m$^{-2}$ in clear-sky and all-sky conditions, respectively. Myhre (2009) estimated the anthropogenic aerosol DRF of $-0.3$ W m$^{-2}$, with an uncertainty of $-0.2$ W m$^{-2}$, by combining a global aerosol model and satellite observations.

Quantitatively understanding the different aerosol effects on climate through observation is very difficult due to the large spatial variations in aerosol concentrations. An atmospheric general circulation model (AGCM) coupled with an aerosol chemical and transport model is therefore a useful tool with which to study aerosol climate effects. The feedback between climate and aerosols can be considered using an interactively coupled system. Liao et al. (2004) simulated the global annual mean forcing due to all aerosols as $-0.72$ W m$^{-2}$ at the top of the atmosphere (TOA) and $-4.04$ W m$^{-2}$ at the surface. The Laboratoire de Météorologie Dynamique GCM coupled with a multi-component aerosol module was used to estimate the global annual average DRF and got a value of $-1.04$ W m$^{-2}$ at the TOA due to total aerosols in all-sky condition (Reddy et al. 2005). The GISS climate model embedded with a detailed aerosol microphysical scheme, called MATRIX, was used to estimate the net aerosol direct effect of $-1.78$ W m$^{-2}$ at the TOA (Bauer et al. 2010). Posselt and Lohmann (2009) found that the total anthropogenic aerosol effect decreased by 0.5–0.9 W m$^{-2}$ when employing a prognostic rain scheme in the global climate model ECHAM5 which represented a more physical treatment of the warm rain precipitation process. AGCMs coupled with ocean models have also been used to study the effects of aerosols on climate. Allen and Sherwood (2010) showed a large-scale land-sea contrast, with general increases in ocean clouds, and decreases in land clouds due to anthropogenic aerosol. They also indicated that the net solar radiation at the surface would increase if absorbing aerosols decrease mid-level clouds, and this is the dominant effect. Several studies showed that aerosols could decrease the solar flux arriving at the surface, causing surface cooling through direct and indirect effects (Takemura et al. 2005; Kristjansson et al. 2005; Ming and Ramaswamy 2009). Koch et al. (2009) found that the global cooling from aerosol direct and indirect effects was $-0.2$ and $-1.0$°C, respectively. The net aerosol cooling effect was about half as large as the greenhouse gas warming. The obvious local characteristics of aerosol emissions have a significant effect on regional climate (Li et al. 2010). The advection of warmer air heated by BC from South and East Asia over the Himalayas contributes to a warming of about 0.6°C (annual mean) in the lower and mid-troposphere of the Himalayan region (Ramanathan et al. 2007). Vertical redistribution of energy caused by aerosols may change the atmospheric thermodynamics and atmospheric circulation significantly. In monsoon regions, aerosols have an important influence on the monsoon circulation and precipitation (Lau and Kim 2006; Wang et al. 2009a, b). Menon et al. (2002) studied the climate effects of BC aerosols in the Asian monsoon region, and showed that the phenomenon of "northern drought/southern flooding'' that has often occurred in summer during the past 50 years in China may be related to BC aerosols. However, some studies also indicated the BC or carbonaceous aerosols didn't produce the aforementioned precipitation pattern (Gu et al. 2006; Zhang et al. 2009). Liu et al. (2009) simulated the effect of aerosol on monsoon using an aerosol-climate offline GCM, and demonstrated that the

direct effects of sulfate and BC aerosols in China both weakened the East Asian winter and summer monsoons. Ji et al. (2011) also found that the anthropogenic aerosols over South Asia had an impact on the Indian summer monsoon onset and precipitation. Observation showed that increased dust and BC loading from local sources in northern India during late spring may lead to an advance of the rainy periods and subsequently an intensification of the Indian summer monsoon (Lau et al. 2006). Using CALIPSO lidar satellite data, Kuhlmann and Quaas (2010) found that aerosol plumes reduced the pre-monsoon seasonal (March–April–May) average shortwave radiation throughout the Asian monsoon region by between 20 and 30 W $m^{-2}$.

To more accurately estimate the DRF due to aerosols and understand their climatic response, we coupled an AGCM developed by the National Climate Center of the China Meteorological Administration [NCC/CMA; the Beijing Climate Center (BCC) BCC_AGCM2.0.1; Wu et al. 2008] to a size-segregated multi-component aerosol module [the Canadian Aerosol Module (CAM)] developed by Gong et al. (2002, 2003). We simulated the optical properties of typical aerosols and compared the results to Aerosol Robotic Network (AERONET) and China Aerosol Robot Sunphotometer NETwork (CARSNET) observations. The DRF of aerosols and their effects on East Asian climate are discussed based on the above coupled model. Both of sea surface temperature (SST) changes and aerosols have important effects on the Asian monsoon (Lestari and Iwasaki 2006; Randles and Ramaswamy 2008). The advantage of this work is that the coupling AGCM is used with an interactive aerosol model and a slab ocean model, which allow the responses of aerosol to climate changes and responses of SSTs to aerosol forcing comparing with the previous studies by Lau et al. (2006), Gu et al. (2006), Chung and Ramanathan (2006), Randles and Ramaswamy (2008), and Liu et al. (2009) who used either the prescribed aerosol masses or AODs or SSTs.

Section 2 introduces the BCC_AGCM2.0.1, the CAM, and our numerical experimental design. Section 3 shows the global distributions of different species of aerosol column burden and optical properties simulated by the coupled model and compares them to observations. The DRF of aerosols and their effects on East Asian summer climate are also described. Finally, the discussion and summary are given in Sect. 4.

## 2 Model description and experimental design

### 2.1 Atmospheric general circulation model

The BCC_AGCM2.0.1 was developed by the NCC/CMA based on the Community Atmosphere Model Version 3 (CAM3) developed by the National Center for Atmospheric Research (NCAR). In this study BCC_AGCM2.0.1 was coupled with a slab ocean model which is from Hansen et al. (1984). The model uses horizontal triangular truncation at wavenumber 42 (T42, approximating 2.8° × 2.8°) and vertical hybrid $\sigma$-pressure coordinates similar to CAM3, which includes 26 vertical layers with the top layer at a pressure of 2.9 hPa. The shortwave radiation is parameterized by a 19-spectral-band scheme that uses a two-stream $\delta$-Eddington approximation (Briegleb 1992). The cloud fraction was derived from diagnostic relationships introduced by Slingo (1987), with variations described by Hack et al. (1993), Kiehl et al. (1998), and Rasch and Kristjansson (1998). The parameterization of non-convective cloud processes has been described by Rasch and Kristjansson (1998), with updates by Zhang et al. (2003). The shallow and upper-level convection used the parameterization from Hack (1994). The radiation parameterization of liquid water clouds was taken from the scheme given by Slingo (1989). Monthly mean climatological data from 1971 to 2000 on a Gaussian grid, obtained from the National Centers for Environmental Prediction (NCEP) reanalysis products, were used as the initial model state. The geographical distribution of sea surface temperature was prescribed based on the 21-year (1981–2001) climatology (available online from http://www/ccsm.ucar.edu/models/atmcam/docs/description).

Compared to CAM3, a few improvements have been implemented in BCC_AGCM2.0.1. The dynamics in the model differs significantly from the Eulerian spectral formulation of the CAM3, and reference stratified atmospheric temperature and surface pressure were introduced into the governing equations to improve calculation of the pressure gradient force and the gradients of surface pressure and temperature (Wu et al. 2008). The major modifications to the model physics included a new convection scheme (Zhang and Mu 2005), a dry adiabatic adjustment scheme in which potential temperature is conserved (Yan 1987), a modified scheme to calculate sensible heat and moisture fluxes over open ocean that considers the effect of ocean waves on latent and sensible heat fluxes (Wu et al. 2010), and an empirical equation to compute the snow cover fraction (Wu and Wu 2004). The model provides overall improvements to climate simulations in comparison to CAM3, especially for simulating the tropical maxima/subtropical minima of precipitation, wind stress, and sensible and latent heat fluxes at the ocean surface (Wu et al. 2010).

### 2.2 Aerosol module

The Canadian Aerosol Module (CAM), a size-segregated multi-component aerosol algorithm, was developed by Gong et al. (2002, 2003). It includes processes for the

emission, transport, chemical transformation, cloud interaction, and deposition of atmospheric aerosols. Five aerosol species were taken into account, including sulfate, BC, OC, soil dust, and sea salt. We used updated source emissions that were derived primarily from AeroCom data. These included the surface emission rate of both natural and anthropogenic aerosols: BC and OC (Van der Werf et al. 2004; Bond et al. 2004), $SO_2$ and sulfate (Van der Werf et al. 2004; Cofala et al. 2005), and dimethyl sulfide (DMS; Kettle and Andreae 2000 for ocean data; Nightingale et al. 2000 for air-sea transfer). Additional emission data were obtained from the Emission Database for Global Atmospheric Research (EDGAR) version 3.2, 1995, database (Olivier et al. 2002; http://www.mnp.nl/edgar). The sea salt module was developed by Gong et al. (2002), and the soil dust scheme was from Marticorena and Bergametti (1995). The model included an online sulfur chemistry module, in which $H_2S$, DMS, $SO_2$, and $H_2SO_4$ are prognostic variables, but the concentrations of OH, $O_3$, $H_2O_2$, and $NO_3$ are prescribed offline from the MOZART/NCAR model (Brasseur et al. 1998; Hauglustaine et al. 1998).

There are two common methods for representing particle size distributions in models: the modal and sectional representations. In the modal representation, each aerosol is represented by an analytical modal distribution function (e.g., Binkowski and Shankar 1995; Ghan et al. 2001). In the sectional representation, the aerosol size distribution is generally approximated by a set of contiguous, non-overlapping, and discrete size bins (e.g., Gong et al. 1997; Jacobson 1997; Meng et al. 1998). This representation of aerosol size distribution is used for its flexibility in treating processes including multi-component interactions such as coagulation, condensation, and chemistry (Gong et al. 2003). The concentrations and optical properties of aerosols can be calculated more accurately according to the given size bins. In our model, the aerosol size spectrum was divided into 12 bins with radii between 0.005–0.01, 0.01–0.02, 0.02–0.04, 0.04–0.08, 0.08–0.16, 0.16–0.32, 0.32–0.64, 0.64–1.28, 1.28–2.56, 2.56–5.12, 5.12–10.24, and 10.24–20.48 μm. The effective radius of the aerosols was taken as the average value in each bin. The hygroscopic growth of soluble aerosol particles was also taken into account. The aerodynamic size of the particles was taken from Kohler theory to be in equilibrium with the ambient relative humidity. A cloud module with explicit microphysical processes was incorporated to simulate cloud droplet activation and subsequent aerosol-cloud-raindrop interaction, as well as cloud chemistry. Within a size bin, internally mixed aerosols were assumed for all aerosol types except the freshly emitted (at the source grid) insoluble components (BC and soil dust). These were assumed to be externally mixed for one integration time step in each grid cell. The number densities of externally mixed components were calculated at every time step in the source grid and then used to obtain the externally mixed aerosol activation and radiative forcing (Ayash 2007).

### 2.3 Optical properties of aerosol

The aerosol optical properties (extinction coefficient, single scattering albedo, and asymmetry parameter) were calculated using Mie scattering theory. The refractive indices of dry aerosols were adopted from D'Almeida (1991), and the Mie scattering code of Wiscombe (1980) was used. Table 1 lists the refractive indices and densities of dry aerosols.

Sulfate, OC, and sea salt particles are hygroscopic, and therefore their size distribution and particle shape may change when they are mixed with water vapor in the ambient air. This can lead to alterations of their refractive indices and corresponding radiative properties. Figure 1 shows the radius growth of the three species of hygroscopic aerosol particles with increasing relative humidity calculated according to Kohler theory. In this calculation, the relative humidity is first divided into 10 bins: 0.0, 0.45, 0.5, 0.6, 0.7, 0.8, 0.9, 0.95, 0.98, and 0.99. Then the radii of wet aerosol particles in each size bin are obtained for these relative humidity bins. The wet particle densities and refractive indices consisting of real and imaginary parts are obtained according to volume-weighted method, respectively. New size-segregated aerosol optical properties, namely the extinction coefficient, single scattering albedo, and asymmetry parameter, were calculated for all 19 spectral bands and each of the 10 relative humidity bins using Mie scattering theory (Wiscombe 1980). These were then incorporated into the BCC_AGCM2.0.1 instead of the original bulk scheme. Therefore, the aerosol optical properties for any relative humidity at each time step could be obtained through linear interpolation. Finally, the optical depth of each aerosol type for each spectral band was calculated according to formula by Liou (2004).

### 2.4 Experimental design

Our aim was to explore the effects of three types of aerosols mainly produced by human activities including sulfate, BC, and OC on East Asian summer climate, including both

**Table 1** The refractive index and densities of dry aerosols

| Component | Refractive index ($\lambda = 0.55$ μm) | Density (kg $m^{-3}$) |
|---|---|---|
| Sulfate | $1.43–1.0 \times 10^{-8}\ i$ | 1,769.0 |
| BC | $1.75–0.44\ i$ | 1,500.0 |
| OC | $1.53–0.0059\ i$ | 1,300.0 |
| Dust | $1.53–0.008\ i$ | 2,650.0 |
| Sea salt | $1.5–9.7 \times 10^{-9}\ i$ | 2,170.0 |

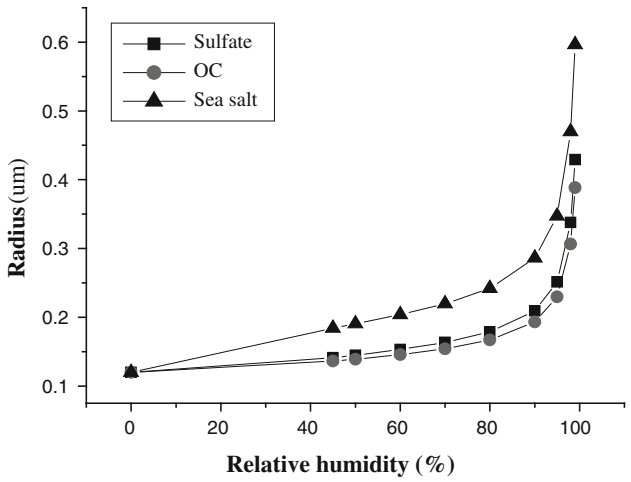


**Fig. 1** The radius growth of the three species of hygroscopic aerosol particles with increasing relative humidity

direct and semi-direct effects. To this end, two experiments were conducted: (*i*) all five species of aerosol were considered (EXP1); (*ii*) only soil dust and sea salt aerosols were included (EXP2). The differences between the results of EXP1 and EXP2 (EXP1 minus EXP2) were regarded as the effects of sulfate, BC and OC aerosols on the climate. In each experiment, the interactive system coupling the BCC_AGCM2.0.1 and CAM has run for 60 years. There was a spin-up period covering the first 30 years, during this period the climate gradually changes. But after that, the simulated climatology had reached a new equilibrium, and we consequently analyzed the last 30 years of each 60-year simulation. The instantaneous DRFs due to total aerosols and individual species were calculated in an additional experiment. Only radiative forcing is estimated with the prescribed SSTs and sea ice according to the general method of calculating the radiative forcing with AGCMs (Hansen et al. 2002; Takemura et al. 2005).

## 3 Results

### 3.1 Global distribution of simulated aerosol column burden

Figure 2 shows the global distributions of annual mean column burden of simulated sulfate, BC, OC, soil dust, and sea salt compared with AEROCOM_MEDIAN (Textor et al. 2006; Schulz et al. 2006; Kinne et al. 2006). The main precursors of sulfate aerosol were $SO_2$, volcanic eruptions, and biological sources, especially the DMS oxidation of marine plankton. The maximum values of sulfate aerosol column burden were mainly located in East Asia, especially south, east, and north China, as well as southeastern U.S., Europe, and India. The maximum burden value was about 10 mg $m^{-2}$ (Fig. 2a). The high sulfate aerosol column burden in these continental areas is attributable to their large industrial $SO_2$ emissions. Over oceans, there was an extended distribution of sulfate aerosols due to long-distance transport of terrestrial sulfate and marine DMS oxidation. The simulated global annual mean sulfate column burden was 1.74 mg $m^{-2}$.

BC is produced from the incomplete combustion of hydrocarbons, including fossil fuels, biofuels, and biomass. Maximum BC column burdens appeared over Asia and central Africa with a maximum value of approximately 1.4 mg $m^{-2}$ (Fig. 2b). These regions have recently experienced rapid urbanization and industrialization, which have triggered soaring carbon consumption by increasing populations and intense traffic emissions. Secondary high values of 0.8 mg $m^{-2}$ were located in parts of India-Bengal and central South America. In contrast, there was comparatively little BC column burden in southeastern U.S., western Europe, and Australia. The simulated global annual mean of BC column burden was 0.14 mg $m^{-2}$.

OC is produced during the complete combustion of biomass or fossil fuels. The highest column burdens of OC occurred in the central regions of South America and Africa, with a maximum burden exceeding 18 mg $m^{-2}$ in Africa (Fig. 2c). This may be caused by the full combustion of carbonaceous material due to the dry conditions in the tropics. There were also obvious OC concentrations over Southeast Asia, India, Australia, and southeastern U.S. The simulated OC concentrations were low in Europe, mainly because secondary organic aerosols, the primary components of OCs, were not taken into account in our model. The simulated global annual mean of OC column burden was 1.31 mg $m^{-2}$.

The dust column burdens were mainly located in the North African Sahara region and West Asia, with a maximum value as high as 1,000 mg $m^{-2}$ (Fig. 2d). The secondary value of more than 100 mg $m^{-2}$ was located in Inner Mongolia and the Xinjiang region of China. The simulated global annual mean dust column burden was 40.8 mg $m^{-2}$.

The distributions of sea salt aerosol covered almost the entire ocean (Fig. 2e). Large column burdens mainly occurred over the oceans between 30° and 60° in both the Southern Hemisphere (SH) and Northern Hemisphere (NH) with values exceeding 20 mg $m^{-2}$. The simulated global annual mean sea salt column burden was 14.7 mg $m^{-2}$.

Figures 2f–j show the corresponding global distributions of annual mean column burden in AEROCOM_MEDIAN. As can be seen from these figures, the magnitude and distribution of the simulated sulfate, sea salt and dust column burdens generally agreed with those of AEROCOM_MEDIAN, but the simulated dust burdens in Sahara and West Asia and sea salt burdens between 30° and 60°S

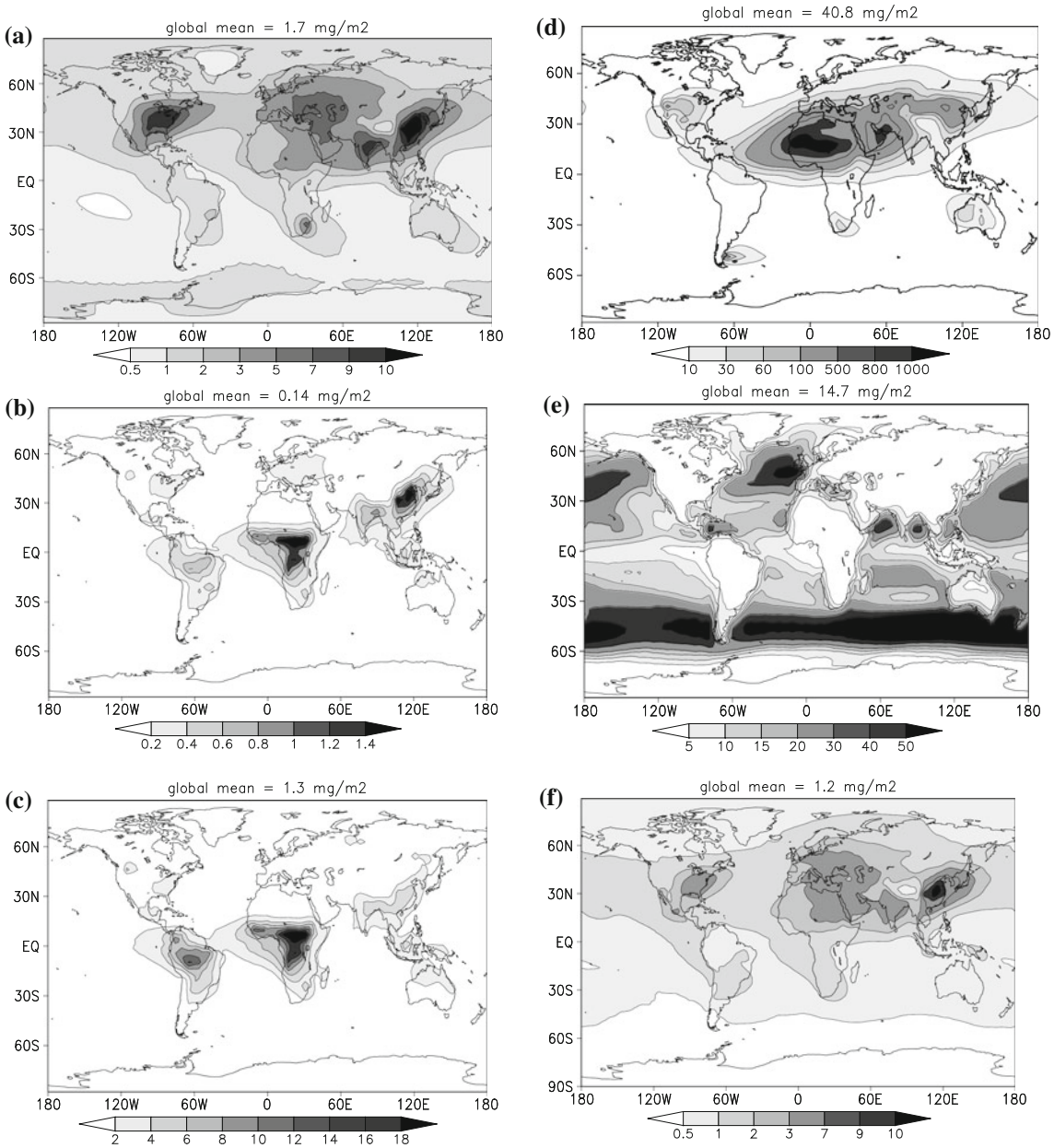


**Fig. 2** The global distributions of annual mean column burden of simulated **a** sulfate, **b** BC, **c** OC, **d** soil dust and **e** sea salt. The **f–j** are the corresponding distributions of AEROCOM_MEDIAN (mg $m^{-2}$)

were larger than the corresponding AEROCOM_MEDIANs. The values and ranges of simulated BC and OC column burdens were smaller than those of AEROCOM_MEDIAN, especially in West Europe, North America and East Asia. Compared with observations and other modeling results (i.e. AEROCOM), the simulated BC and OC concentrations from this model are low and the ratio of dry to wet depositions is different from other models. We have done a series of model experiment to examine the performance of the model. Firstly, we checked the budget information of the model in terms of emission and atmospheric burden. Table 2 is a summary of the budget information for a number of reference models. For example, the emission of BC in our model is just a little over half of GISS model (Koch 2001), and the atmospheric burden of BC from our model is also about half of that for GISS model. And compared with the IPCC-TAR, the BC emission in AEROCOM is lower (Dentener et al. 2006). It seems that the BC and OC bias from our model is largely from the emission underestimation compared with other models. Furthermore, all types of aerosols are treated as the internal mixture in this model and their wet depositions are calculated with the same parameterization scheme. In reality, due to its hydrophobic nature, BC should be less

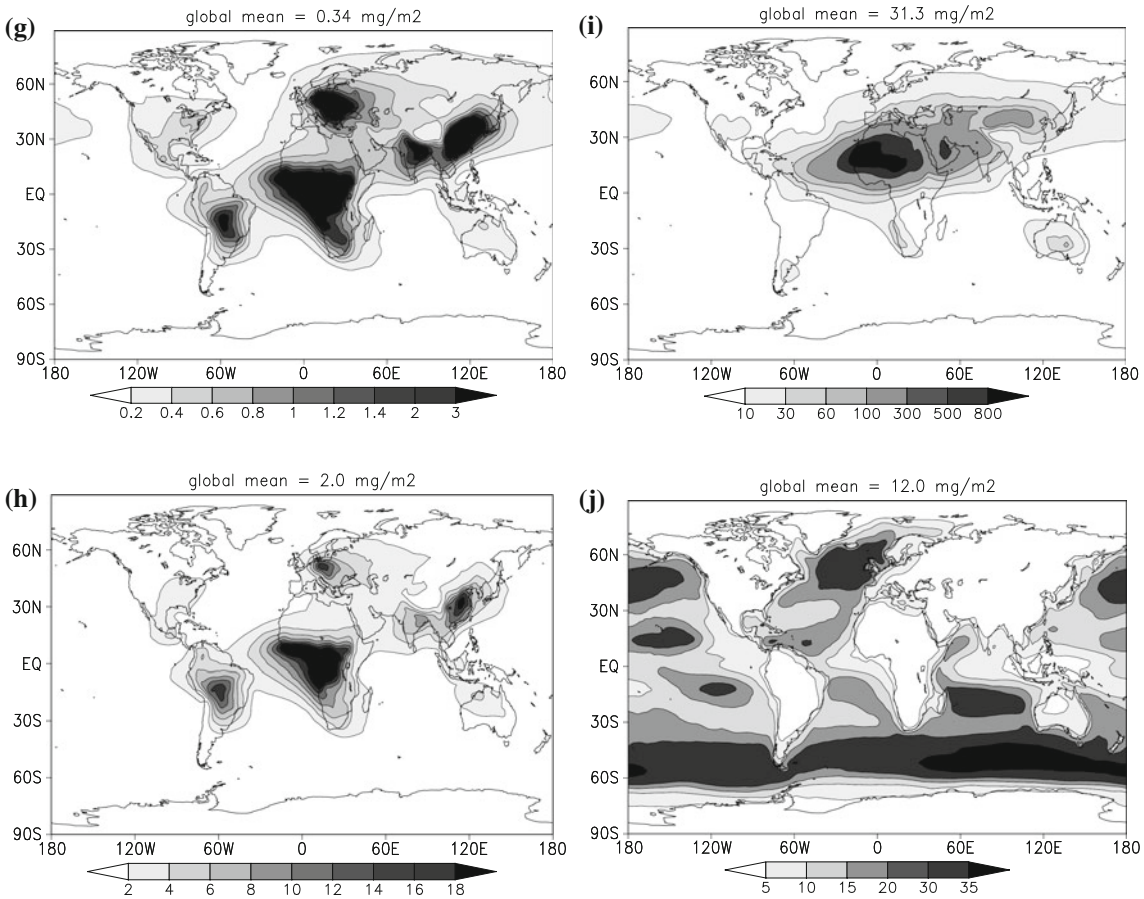


**Fig. 2** continued

**Table 2** Summary of the global emission and burden of BC

| Model | Emission (Tg year$^{-1}$) | Burden (Tg) | References |
|---|---|---|---|
| Our study | 7.7 | 0.07 | Dentener et al. (2006) |
| GISS | 12.41 | 0.14 | Koch (2001) |
| MIRAGE | 14.0 | 0.22 | Easter et al. (2004) |
| LMDZT | 10.5 | 0.19 | Reddy et al. (2005) |
| GOCART | 13.7 | 0.27 | AEROCOM |
| PNNL | 11.4 | 0.19 | AEROCOM |
| IPCC-TAR | 12.3 | | Dentener et al. (2006) |

The results of AEROCOM are from the website http://nansen.ipsl.jussieu.fr/AEROCOM/data.html

removed by wet deposition than hydrophilic aerosols (i.e. sulfate). This also results in under-estimate of BC concentrations. Additionally, the secondary organic aerosols (SOAs) are not included in our model which can lead to underestimation of simulated OC concentration. As to the dry to wet deposition ratios, we found that the difference was from the size distributions of primary emissions of BC and OC. The change of the primary BC size distribution can change the dry and wet deposition ratios. In this paper, the model uses a sectional representation to simulate the aerosol size distributions with 12 size bins and uses a mass mean diameter (MMD) "0.1 um" as the size distribution of primary BC emissions. After we changed the MMD to 0.24 um, the ration of dry to wet deposition has been changed to the value similar to most of other models (Table 3).

### 3.2 Simulated aerosol optical properties

Figure 3a shows the global annual mean distribution of the simulated total AOD at 550 nm. The highest AOD values (0.4–0.7) were found over the Sahara Desert, followed by

**Table 3** The global budget of BC for different mass mean diameter (MMD)

| MMD (um) | Burden (Tg) | Emission (Tg year$^{-1}$) | Dry deposition (%) | Wet deposition (%) |
|---|---|---|---|---|
| 0.1 | 0.07 | 7.7 | 59 | 41 |
| 0.24 | 0.071 | 7.7 | 29 | 71 |

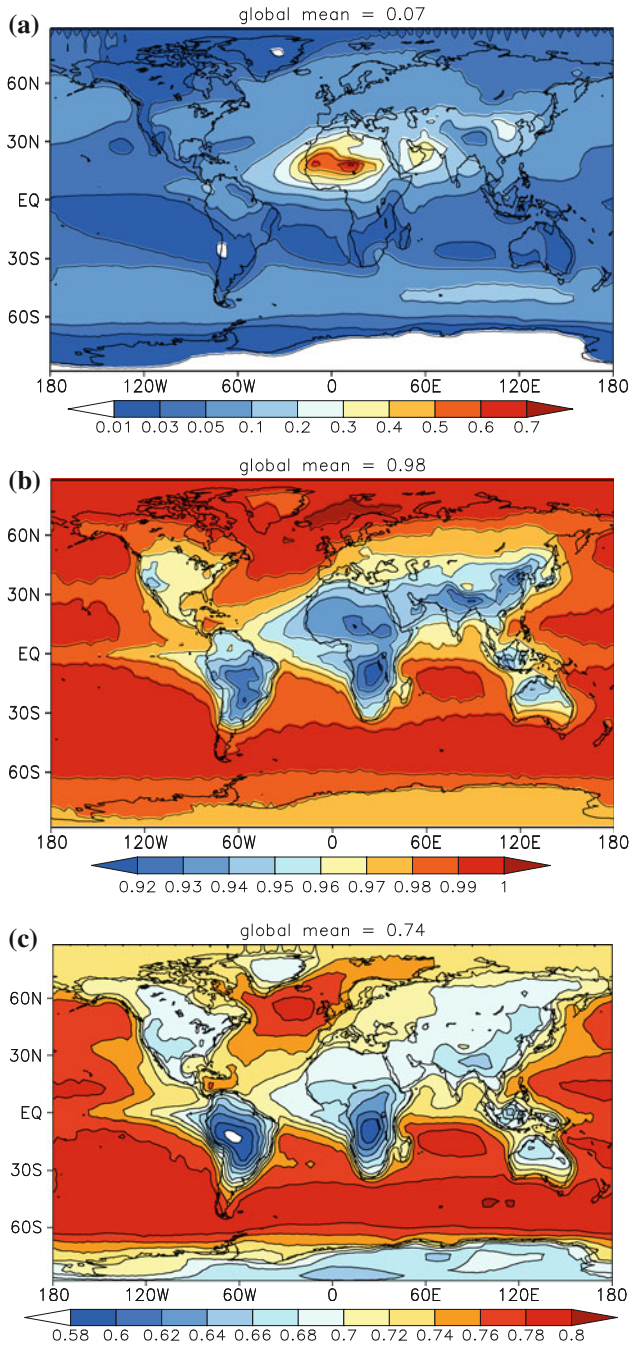


**Fig. 3** The global annual mean distributions of simulated **a** total AOD, **b** single scattering albedo and **c** asymmetry parameter at 550 nm

Arabia in West Asia (0.2–0.4). These were both due to the large contribution from soil dust. The AODs in east China were usually more than 0.1. They reached a maximum value of more than 0.2 in north China, which was larger than that for most other continental areas, except for those mentioned above. The AOD values were around 0.1 in developed countries such as those in North America and west Europe and ranged from 0.05 to 0.1 over the oceans between 30° and 60° in both hemispheres, due to the contributions from sea salt and sulfate. In terms of the global mean, soil dust aerosols had the largest optical depth (0.028), followed by sea salt (0.026), sulfate (0.01), OC (0.005), and BC (0.0006). Figure 3b, c represent the global annual mean distributions of simulated single scattering albedo and the asymmetry parameter at 550 nm for all aerosols, respectively. The single scattering albedos were around 0.92 and the asymmetry parameters were in the range of 0.58–0.66 in East Asia, South Asia, and South America, where carbonaceous aerosols are a major aerosol component, and in North Africa and West Asia, where the soil dust is dominant. However, in North America, where the sulfate burden is high, the single scattering albedo and asymmetry parameter were around 0.96 and 0.68, respectively. This was also the case in Europe, where the two variables were around 0.97 and 0.7, respectively. Over oceans, the single scattering albedo approached 1.0, and the asymmetry parameters ranged from 0.74 to 0.9 due to the scattering effect of sea salt aerosols.

Figure 4 compares the monthly mean AODs between the simulation and measurement from CARSNET at six sites: Beijing (116.5°E, 39.8°N), Lin'an (119.73°E, 30.3°N), Pudong (121.5°E, 31.3°N), Dunhuang (94.7°E, 40.15°N), Ejinaqi (101.1°E, 42°N), and Lasa (91.1°E, 29.7°N). The simulated values were close to the minimum limit of observations at Beijing and Dunhuang, and the magnitude and seasonal variation of simulated AODs agreed closely with the observations at Ejinaqi. However, the simulated values were lower than the observed values at Lin'an, Pudong, and Lasa, which can partially be attributed to the lack of nitrate and ammonium aerosols.

The simulated total AODs were compared with the ground-based sun photometer measurements from AERONET in Fig. 5. Figure 5a–c show comparisons at sites in

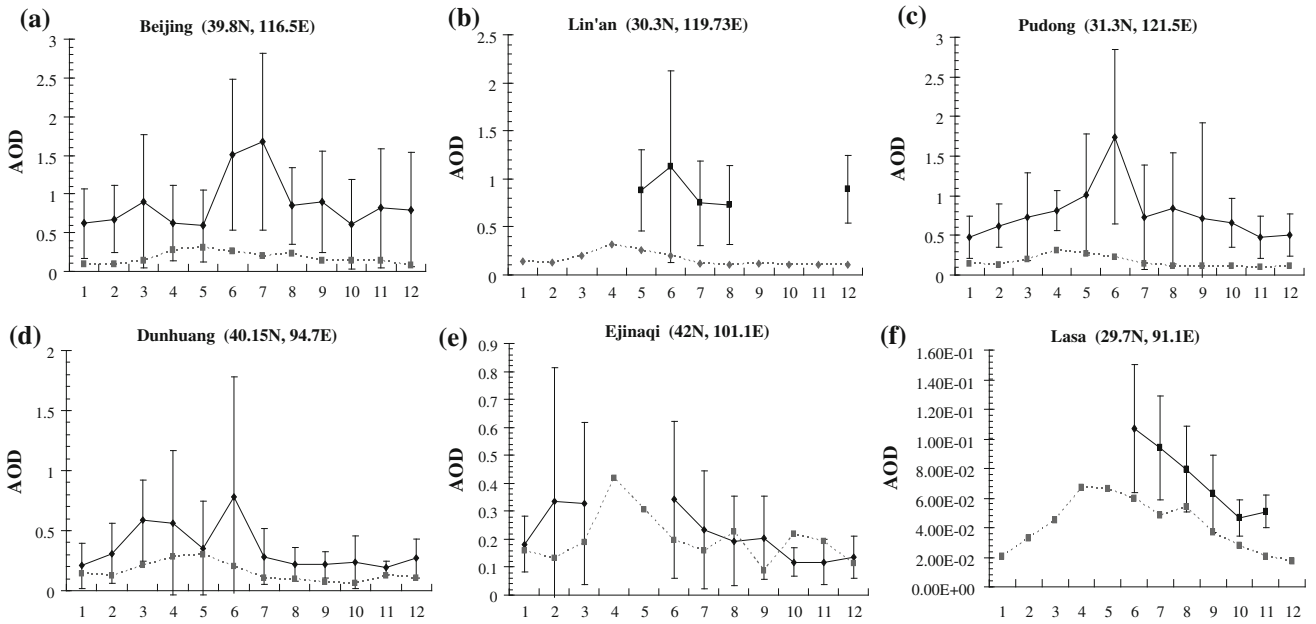


**Fig. 4** Comparisons of simulated total AOD (*dashed line*) with those measured (*solid line*) at 6 CARSNET sites at 550 nm. The *error bar* indicates the standard deviation of observed optical depth. The CARSNET data are from China Meteorological Administration Aerosol Remote Sensing NETwork

East Asia. The modeled total AODs over Beijing (116.3°E, 40°N) and Gosan (126.2°E, 33.3°N) agreed reasonably with measurements of seasonal variation. Both showed higher magnitudes in spring and summer, which were slightly higher than the minimum limit of the observed values at these sites. The simulated values in Osaka (135.6°E, 34.7°N) were lower than the observations in spring and summer, most likely because of the weaker transport of aerosols from China and omission of nitrate and ammonium aerosols in the model.

Figure 5d–h compare the modeled and measured AODs at the sites that were mainly influenced by soil dust aerosols. As can be seen from the comparison of the Hamin (54.3°E, 23°N) site in West Asia, the model could capture the seasonal variations fairly well, including a peak from June to August. However, the simulated values were higher in summer (July) and lower in winter than those of AERONET. The magnitude and seasonal variation of the simulated AODs agreed closely with those observed at Dalanzadgad (104.4°E, 43.6°N) in Mongolia and at the IER_Cinzana (5.9°W, 13.3°N), Saada (8.2°W, 31.6°N), and La_laguna (16.3°W, 28.5°N) sites in Africa. However, the values were slightly higher than the maximum limit of observations at La_laguna in spring.

Figure 5i–k exhibited similar properties at three sites in Europe that were mostly affected by sulfate: Venice (12.5°E, 45.3°N), Davos (9.8°E, 46.8°N), and Laegeren (8.4°E, 47.5°N). The magnitude and seasonal variation of simulated AODs agreed well with the observations at Davos, and the simulated values were close to the minimum limit of observations at Venice and Laegeren. The deviations of simulations from observed values in Europe were also partially due to SOAs being ignored in the model.

Figure 5l–n show comparisons at sites in North America where sulfate and dust aerosols dominate. As can be seen for Ames (93.8°W, 42°N), Bondville (88.4°W, 40°N), and Sevilleta (106.9°W, 34.4°N), the simulated AODs agreed reasonably with measurements from November to March, but approached the minimum limit of the observations in other months. At the same time, the model tended to underestimate AODs in South America (Fig. 6o, p), likely because of the low carbonaceous aerosol emissions shown by the model in that region.

Finally, Fig. 5q, r give AODs for remote oceanic sites: Dunedin (170.5°E, 45.9°S) and Lanai (156.9°W, 20.7°N). The model system reproduced the seasonal variations of AODs well, but it obviously overestimated the AOD at Dunedin during May and September and underestimated the values at Lanai between April and June. The AODs of other months were in the range of the measurements.

Figure 6 summarizes the comparisons of the single scattering albedo and asymmetry parameter between the simulations and observations at 52 AERONET sites at 550 nm. The biases of the simulated single scattering albedos were less than 0.04 at most sites, with overestimation in general (Fig. 6a). The mean difference between simulated and observed single scattering albedos was 4%, but extreme deviations exceeded 7% at some sites in western Europe, North and South America and northern

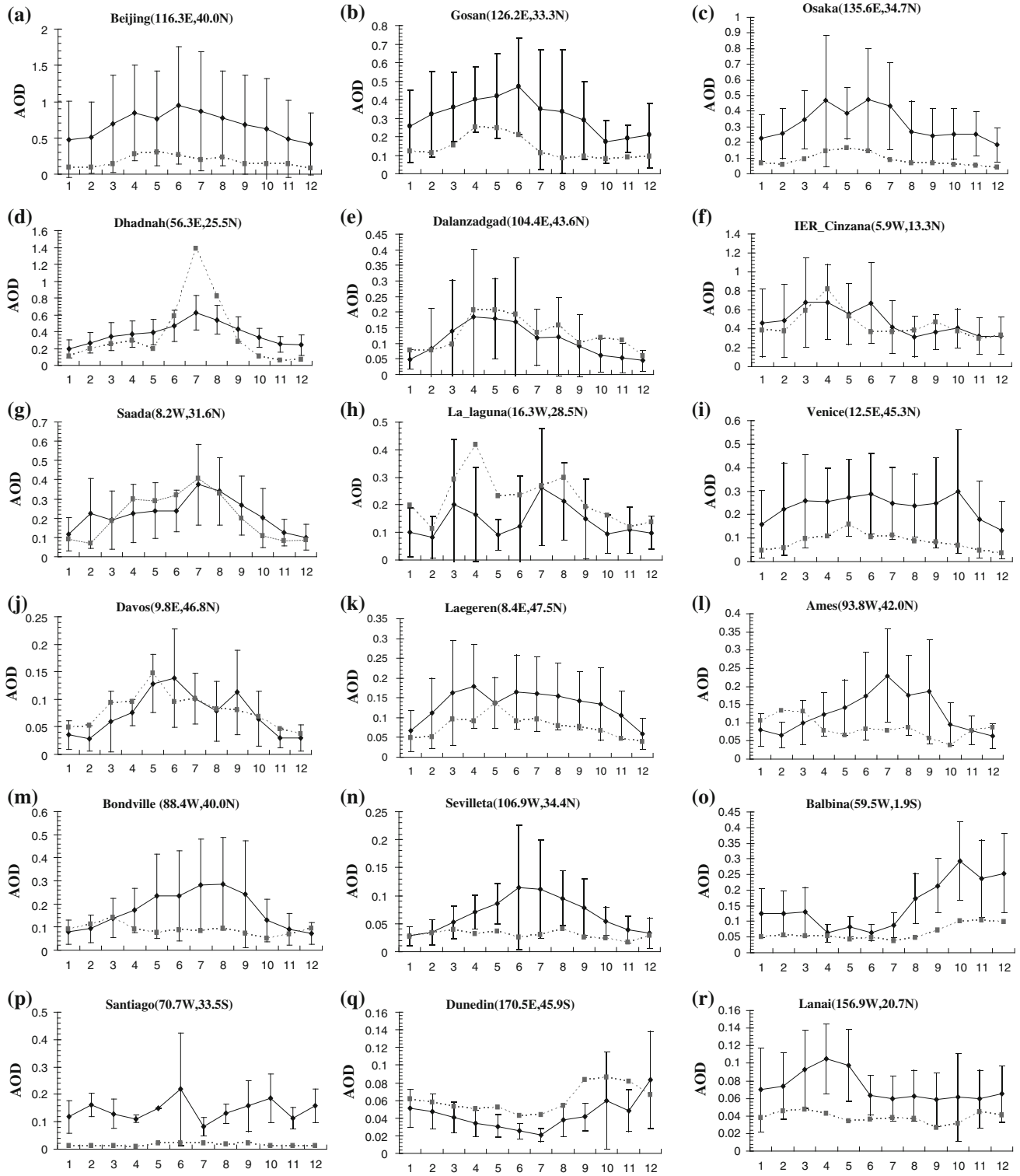


**Fig. 5** Same as in Fig. 5 but for AERONET observations

Africa due to the underestimation of the BC concentration. The model simulated the asymmetry parameters well, with reasonable agreement with measurements (Fig. 6b). The mean difference between the simulated and observed asymmetry parameters was 5%, with the largest biases around 10% at some sites in Africa.

The errors in the above comparison were caused by various factors, including errors in the source emissions,

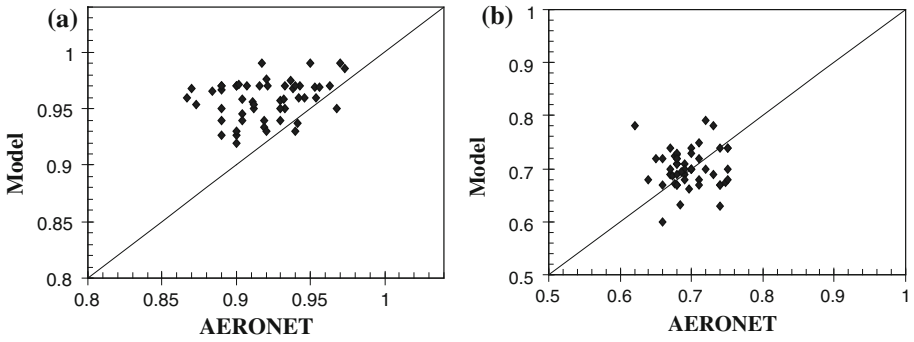


**Fig. 6** Scatterplots of the simulated **a** single scattering albedo and **b** asymmetry parameter versus AERONET at 52 sites at 550 nm

observational instruments, limitations in the model resolution and the implementation of physical processes in the model. In addition, nitrate and ammonium aerosols and SOAs were not included.

### 3.3 Direct radiative forcing of aerosols

Instantaneous radiative forcing calculations were performed online with the AGCM-aerosol coupled system. Figure 7 shows the annual mean distributions of the simulated DRF of each aerosol species at the TOA under all-sky and clear-sky conditions. Generally, sulfate aerosols caused negative radiative forcing at the TOA due to their strong scattering under all-sky conditions (Fig. 7a). The highest DRFs of sulfate, with a maximum value exceeding $-1.0$ W m$^{-2}$, occurred in East Asia and North America due to large industrial emissions of $SO_2$ and sulfate particles. The second strongest DRFs were about $-0.5$ W m$^{-2}$ in India and western Europe. Long-distance transport of sulfate aerosols from the continent and the oxidation of DMS in the ocean caused negative forcing over the ocean. The simulated global annual mean of sulfate DRF at the TOA was $-0.19$ W m$^{-2}$, which was consistent with the estimations of $-0.19$ W m$^{-2}$ by Koch (2001) and $-0.21$ W m$^{-2}$ by Takemura et al. (2005).

BC can absorb solar radiation, generating positive radiative forcing at the TOA under all-sky conditions (Fig. 7b). The region with the largest DRF was East Asia, especially south and east China, where the maximum value reached approximately $+1.0$ W m$^{-2}$. The large DRF of BC in that region was mainly caused by local fossil fuel and biomass burning. The DRFs exceeded $+0.5$ W m$^{-2}$ in most of central Africa and were attributable to the natural burning of carbonaceous materials. BC DRFs were mainly above $+0.1$ W m$^{-2}$ in western Europe, eastern U.S., and South America. There was also positive forcing at the high latitudes of more than 60°N, resulting from long-distance transport of BC emitted at lower latitudes. The simulated global annual mean of BC DRF at the TOA was $+0.1$ W m$^{-2}$, close to the results of $+0.08$ W m$^{-2}$ estimated by Pitari et al. (2002) but much smaller than the $+0.32$ W m$^{-2}$ reported by Takemura et al. (2005) and $+0.61$ W m$^{-2}$ estimated by Hansen et al. (2005). In this study, the assuming external mixing states of black carbon aerosols could potentially lead to an underestimate of BC forcing (Bond and Bergstrom 2006).

The main optical property of OC is its scattering of solar radiation. This results in negative DRF at the TOA under all-sky conditions (Fig. 7c). The distributions of the DRF of OC were basically consistent with those of BC but with negative values. The largest DRFs of OC occurred in central Africa, where maximum values exceeded $-1.0$ W m$^{-2}$. Other regions with large OC DRF included South America, Southeast Asia, North America, and Europe. DRFs in these regions were generally between $-0.2$ and $-1.0$ W m$^{-2}$. The transport distance of OC is generally much farther than that of BC because of the strongly hydrophilic properties of OC. This implies that the spatial extent of the forcing due to OC is larger than that of BC. The simulated global annual mean of OC DRF at the TOA was $-0.15$ W m$^{-2}$, which agreed closely with the results of $-0.18$ W m$^{-2}$ estimated by Chung and Seinfeld (2002), $-0.14$ W m$^{-2}$ by Koch (2001), and $-0.1$ W m$^{-2}$ by Takemura et al. (2005).

Soil dust is another kind of aerosol that scatters solar radiation. It usually causes negative DRF at the TOA under all-sky conditions (Fig. 7d). However, the absorbing effect of dust on longwave radiation was not considered in this work. The largest forcing mainly occurred over West Asia, north China, and especially northern and western Africa. In those regions, maximum forcing exceeded $-10$ W m$^{-2}$ because of the large dust loading, high surface albedo, and abundance of large-scale stratus clouds that cause multiple scattering of solar radiation (Schumacher and Houze 2006). The simulated global annual mean DRF of dust at the TOA was $-0.9$ W m$^{-2}$, which was smaller than those of AEROCOM models (e.g. $-0.75$ W m$^{-2}$ by GISS, $-0.6$ by LSCE, and $-0.54$ by UMI; IPCC 2007).

Sea salt aerosols produced negative forcing globally at the TOA under all-sky conditions because of their scattering properties (Fig. 7e). The largest forcing by sea salt occurred over the oceans between 30° and 60° in both

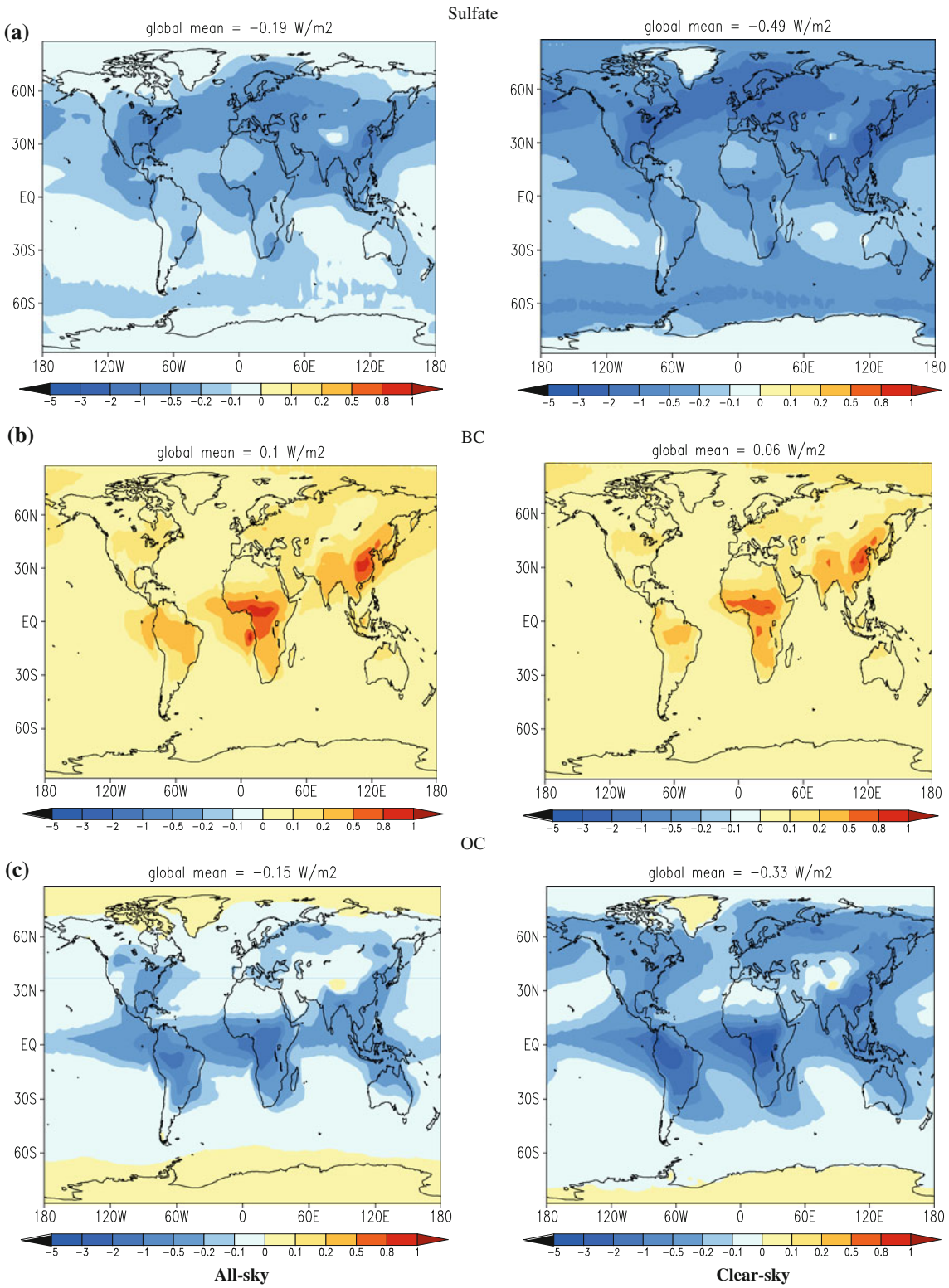


**Fig. 7** Annual mean distributions of the simulated DRF (W $m^{-2}$) due to **a** sulfate, **b** BC, **c** OC, **d** soil dust and **e** sea salt at the TOA under all-sky (*left*) and clear-sky (*right*) conditions

hemispheres. The maximum cooling of −2.0 W $m^{-2}$ in the model was very similar to the results obtained by Liao et al. (2004). The simulated global annual mean DRF of sea salt at the TOA was −0.83 W $m^{-2}$. However, there are still large uncertainties in sea salt forcing, and previous estimates of the global annual mean of this forcing range from

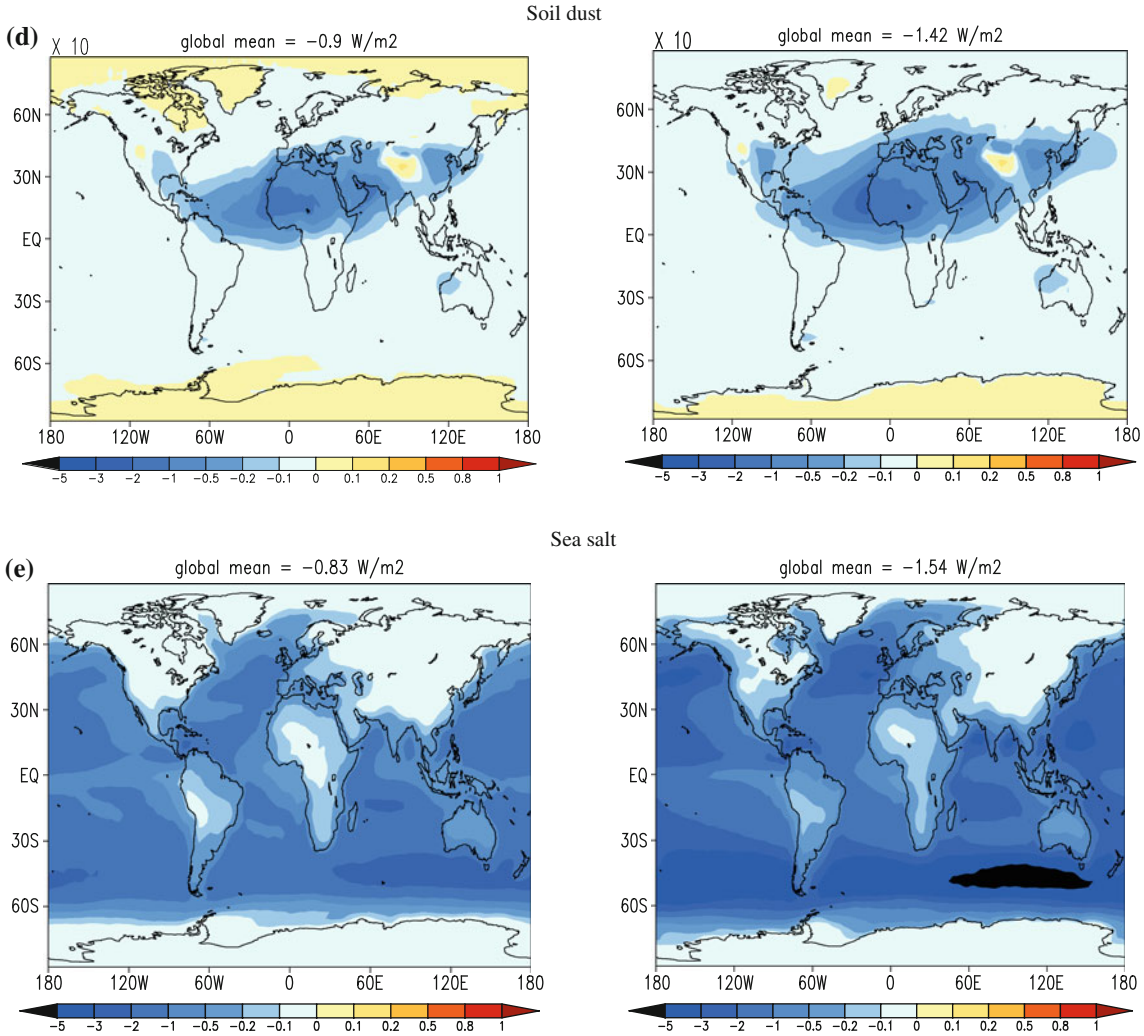


**Fig. 7** continued

−0.31 (Takemura et al. 2002) to −1.1 W $m^{-2}$ (Grini et al. 2002).

The strength and extension of the DRF due to various scattering aerosols may be less under all-sky conditions than under clear-sky conditions, as seen in Fig. 7. However, the sign of the forcing becomes opposite for absorbing aerosols such as BC. Therefore, it is concluded that the presence of clouds can enhance positive forcing and weaken negative forcing at the TOA, which is consistent with the results of Zhang et al. (2009). Table 4 lists the simulated annual hemispherical and global mean DRF by each species of aerosol components at the TOA and surface under all-sky and clear-sky conditions. The annual mean DRFs for three types of aerosol mainly produced by human activities including sulfate, BC, and OC were obviously higher in the NH than in the SH, and the DRFs were higher at the surface than at the TOA due to the multiple scattering and absorption of solar radiation by aerosols in the atmosphere. The simulated global annual means of the DRFs at the TOA due to all aerosols and three types of aerosol (sulfate, BC and OC) were −2.03 and −0.23 W $m^{-2}$ under all-sky conditions, respectively.

### 3.4 Effect of sulfate, BC and OC aerosols on the East Asian summer monsoon

The East Asian summer monsoon plays a controlling role in the summer climate in East Asia, where the emissions of sulfate, BC and OC aerosols are the highest in the world. The large aerosol burden inevitably affects the temperature structure and atmospheric circulation by changing the radiation fields and thereby also affects the East Asian summer monsoon and regional climate. The results obtained in this work showed that the summer season (June, July, August: JJA) average DRFs due to the aforementioned three types of aerosol in East Asia (20°–40°N,

**Table 4** Simulated annual hemispherical and global mean DRF due to different aerosol components at the TOA and surface under all-sky and clear-sky conditions (W $m^{-2}$)

| | All sky | | | Clear sky | | |
|---|---|---|---|---|---|---|
| | NH | SH | Global | NH | SH | Global |
| Sulfate | −0.28 (−0.3) | −0.1 (−0.11) | −0.19 (−0.21) | −0.68 (−0.71) | −0.26 (−0.27) | −0.47 (−0.49) |
| BC | +0.12 (−0.24) | +0.06 (−0.15) | +0.1 (−0.19) | +0.09 (−0.32) | +0.03 (−0.18) | +0.06 (−0.25) |
| OC | −0.16 (−0.27) | −0.13 (−0.21) | −0.15 (−0.24) | −0.39 (−0.52) | −0.27 (−0.36) | −0.33 (−0.44) |
| Dust | −1.7 (−3.8) | −0.13 (−0.21) | −0.9 (−1.98) | −2.6 (−4.8) | −0.2 (−0.29) | −1.42 (−2.55) |
| Sea salt | −0.61 (−0.71) | −1.0 (−1.2) | −0.83 (−0.94) | −1.1 (−1.3) | −2.0 (−2.2) | −1.54 (−1.72) |
| Sulfate + BC + OC | | | −0.23 (−0.59) | | | −0.73 (−1.13) |
| All aerosols | | | −2.03 (−3.63) | | | −3.84 (−5.61) |

The values in parentheses represent the corresponding surface forcing

*NH* northern hemisphere, *SH* southern hemisphere

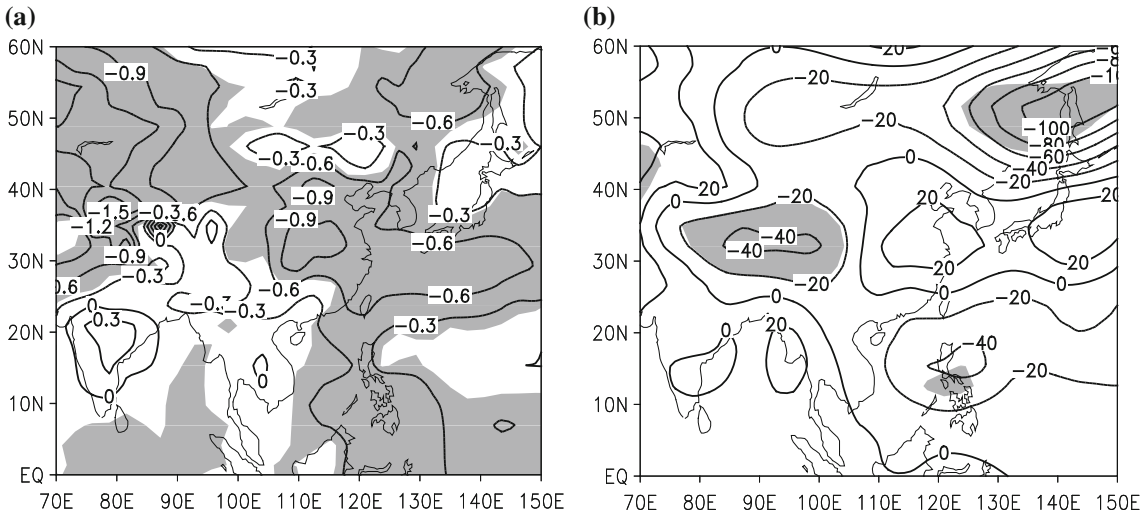


**Fig. 8** The differences of JJA mean **a** surface temperature (°C) and **b** surface pressure (Pa) between EXP1 and EXP2. The *shade* indicates a confidence level of 90% from the *T*-test

100°–140°E) at the TOA and surface were −1.4 and −3.3 W $m^{-2}$, respectively, leading to decreases of 0.58°C and 0.14 mm $day^{-1}$ in the JJA means of surface temperature and precipitation rate in this area, respectively.

Figure 8 shows the changes of the JJA mean surface temperature and surface pressure in East Asian monsoon region due to sulfate, BC and OC aerosols. Any species of aerosol, whether absorbing or scattering, will decrease the solar radiative flux arriving at the surface and hence the surface temperature. A decrease of surface temperature was seen almost everywhere in East Asian monsoon region, but the decrease of surface temperature over land was obviously stronger than that over sea (Fig. 8a). The cooling over land at most areas of East Asia exceeded −0.6°C, especially in north China and central and east China with a magnitude of −0.9°C or so due to the huge loading of aerosols. The cooling in the west Pacific was below −0.6°C. The distribution of surface temperature changes over land basically agreed with the results reported by Liu et al. (2009) which considered the sulfate and BC aerosols in a GCM, whereas the changes over oceans is contrary to the results by Liu et al. (2009) because they used the prescribed SST in their GCM. As can be seen from the change of surface pressure in JJA (Fig. 8b), surface pressure was increased dramatically in the central and east China due to cooling over land, whereas surface pressure over the ocean on the south of China was reduced which could be relative to the changes of wind field and local circulation (Figs. 9, 11). The formation of East Asian summer monsoon is mainly due to contrast of land-sea temperature and pressure. Figure 8 showed that the differences of land-sea surface temperature and pressure were weakened in East Asian monsoon region due to the effect of aerosols, thus leading to the weakening of East Asian

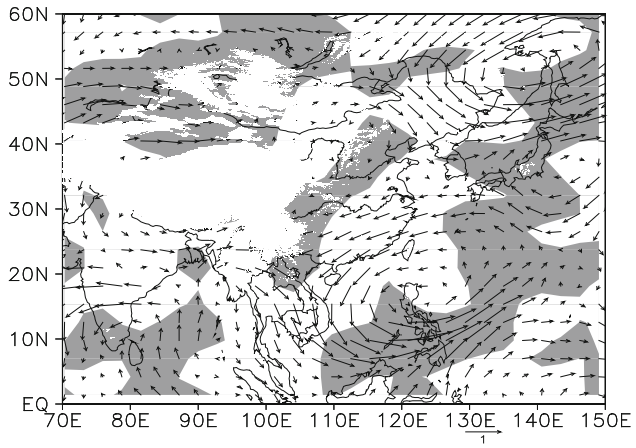


**Fig. 9** The differences of JJA mean wind field at 850 hPa (*vector*) between EXP1 and EXP2. The *shade* shows the differences of moisture flux divergence between EXP1 and EXP2 are negative integrated from 850 to 700 hPa

summer monsoon. The temperature changes are significant at a 90% confidence level in most areas of East Asian monsoon region, whereas the confidence level of pressure changes was not significant here.

East Asian summer monsoon has a typical feature on summer wind field at 850 hPa. The southwest and south winds prevail in south and east China in summer, which carries warm and moist air into China from ocean and induces precipitation. As can be seen from the change of wind field at 850 hPa in JJA (Fig. 9), the enhanced northeasterly flow in south and east China due to sulfate, BC and OC aerosols distinctly weakened the intensity of the southwest summer monsoon, and moreover the moisture flux divergence in lower atmosphere was strengthened. Thus, the monsoon precipitation is suppressed in most areas of south and east China and over the nearby oceans (Fig. 10b). Generally, the increase (or decrease) of surface latent heat flux corresponds to the increase (or decrease) of precipitation. The decrease of surface temperature led to the reducing of surface evaporation and latent heat flux in south and east China (Fig. 10a), which caused less moist air into atmosphere and reduced the precipitation. However, the change of precipitation wasn't consistent with that of surface latent heat flux over the South China Sea, which could mainly caused by the changes of wind field and circulation. A cyclonic circulation formed over the west Pacific and South China Sea at 850 hPa and the moisture flux convergence in lower atmosphere in the south of the cyclonic was obviously strengthened (Fig. 9), which increased the vertical transport of water vapor and precipitation. This indicated that the effect of dynamic on precipitation was predominant over ocean. The changes of precipitation in East Asian monsoon region in this paper were consistent with the results by Lau et al. (2006) due to the effect of five aerosol species including sulfate, BC, OC, soil dust, and sea salt.

Figure 11 shows the changes of JJA mean temperature and vertical meridional circulation zonally averaged between 105°E and 120°E due to the aerosols. The figure clearly indicated the responses of atmospheric dynamic and thermodynamic on the aerosol effects. As can be seen from Fig. 11a, aforementioned three species of aerosol led to the decrease of temperature in whole troposphere, which indicated the total feature of these aerosols was scattering over China. The reduce of temperature in the lower atmosphere was smaller than that in mid and high atmosphere to the south of 15°N which was beneficial to the

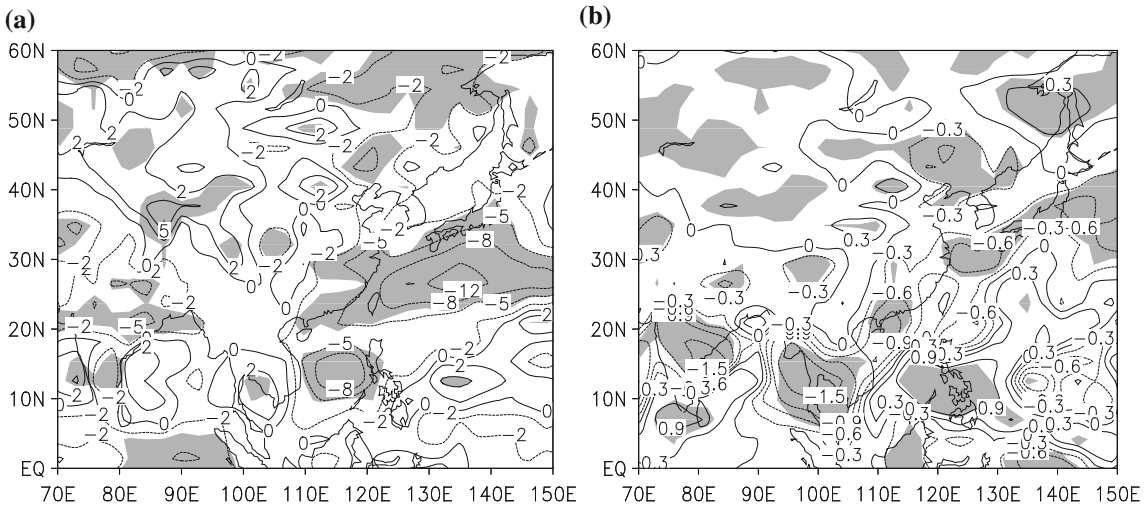


**Fig. 10** The differences of JJA mean **a** surface latent heat flux (W $m^{-2}$) and **b** precipitation (mm $day^{-1}$) between EXP1 and EXP2. The *shade* indicates a confidence level of 90% from the *T*-test

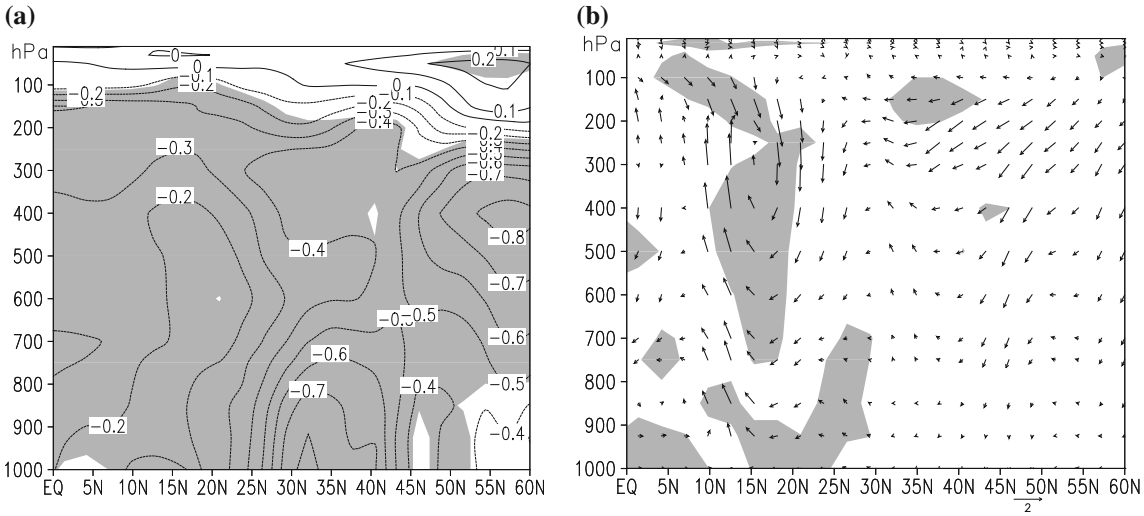


**Fig. 11** The differences of JJA mean **a** temperature (°C) and **b** vertical meridional circulation zonally averaged between 105°E and 120°E between EXP1 and EXP2. The *shade* indicates a confidence level of 90% from the *T*-test

enhancing of vertical ascending motion, whereas the contrary changes occurred between 15°N and 30°N which enhanced the atmospheric stability and suppressed convective motions. The local meridional circulation was changed with the atmospheric temperature changes (Fig. 11b). A clockwise rotation appeared between 10°N and 30°N in which ascending motion developed between 10°N and 15°N and subsidence motion developed between 15°N and 30°N, leading to the weakening of the normal summer meridional circulation here which poses as a counter-clockwise rotation (Liu et al. 2009). The increased subsidence between 15°N and 30°N strengthened the southward motion in lower troposphere, which weakened the northward transport of warm and moist air carried by the East Asian summer monsoon. This result accorded with the changes induced by sulfate reported by Liu et al. (2009). Ultimately, the decrease of moist air and increase of subsidence led to the decrease of monsoon precipitation between 15°N and 30°N in south and east China.

It should be noted that the absorbing BC and scattering OC masses were underestimated obviously in East Asia by this model, which will necessarily affect simulated climatic effect of aerosols over Asia. Menon et al. (2002) showed that absorbing BC aerosol could increase precipitation over southern China and decrease precipitation over northern China. Chung and Ramanathan (2006) indicated that BC aerosol could heat the troposphere and enhance vertical convection over the North Indian Ocean and Indian subcontinent, causing an increase in monsoon precipitation. Randles and Ramaswamy (2008) also found that an enhanced monsoon circulation associated with increased higher absorption aerosol optical depth resulted in the increase of low-level convergence, upward motion, and precipitation, whereas increase of only scattering aerosols weakened the monsoonal circulation and inhibited precipitation. Both of the underestimation of scattering OC and absorbing BC aerosols will have more complicated effects on the local climate of China.

## 4 Conclusions

An interactive coupled climate-aerosol model consisting of the BCC_AGCM2.0.1 and the Canadian Aerosol Module (CAM) was developed at the NCC/CMA. The magnitude and distribution of the simulated sulfate, sea salt and dust column burdens generally agreed with those of AEROCOM_MEDIAN, but the simulated values and ranges of simulated BC and OC column burdens were obviously smaller than those of AEROCOM_MEDIAN, especially in West Europe, North America and East Asia. These biases can be largely from the emission underestimation in our model compared with other models, and moreover the SOAs are not included in our model.

The simulated optical depth, single scattering albedo, and asymmetry parameter of total aerosols (including sulfate, BC, OC, dust, and sea salt) at 550 nm were basically consistent with AERONET observations, except for an obvious underestimation over South America. The mean relative errors of the simulated single scattering albedo and asymmetry parameter against observations were 4% and 5%, respectively. The magnitude and seasonal variation of the simulated AODs agreed closely with CARSNET observations at Ejinaqi, Dunhuang, and Beijing, but the simulated values were slightly lower than observations at Lin'an, Pudong, and Lasa. Ammonium and nitrate aerosols were not included in the present model, which led to lower simulated AODs in some regions and seasons.

The simulated global annual means of DRF due to total aerosols and three types of aerosol including sulfate, BC, and OC at the TOA were $-2.06$ and $-0.23$ W m$^{-2}$, respectively, under all-sky conditions. The global annual means of sulfate, BC, and OC DRF at the TOA were $-0.19$, $+0.1$, and $-0.15$ W m$^{-2}$, respectively. Clouds can decrease the extension and strength of the DRF for scattering aerosols, but increase them for absorbing aerosols such as BC.

The summer seasonal average DRFs due to three types of aerosol (sulfate, BC, and OC) in East Asia at the TOA and surface were $-1.4$ and $-3.3$ W m$^{-2}$, respectively, leading to decreases of 0.58°C and 0.14 mm day$^{-1}$ in the JJA means of surface temperature and precipitation rate in this area, respectively. The differences of land-sea surface temperature and surface pressure were reduced in East Asian monsoon region due to the effect of these aerosols, thus leading to the weakening of East Asian summer monsoon. The enhanced northeasterly flow in south and east China at 850 hPa due to sulfate, BC and OC aerosols distinctly weakened the intensity of the southwest summer monsoon, and suppressed the monsoon precipitation in most areas of south and east China and over the nearby oceans. The local meridional circulation was also affected due to these aerosols, and a clockwise rotation appeared between 10°N and 30°N. The increased subsidence between 15°N and 30°N strengthened the southward motion in lower troposphere, which weakened the northward transport of warm and moist air carried by the East Asian summer monsoon, and moreover decreased the summer monsoon precipitation in south and east China.

In addition, the model also does not simulate nitrate and SOA, both of which are the important components of aerosols in some parts of Asia. The decrease of land surface temperature in some areas may be larger if taking account these scattering aerosols into in this model, which could more significantly weaken East Asian summer monsoon. But it needs further investigations in the next.

**Acknowledgments** This work is financially supported by National Basic Research Program of China (Grants No. 2011CB403405 and 2006CB403707), the Public Meteorology Special Foundation of MOST (Grant No. GYHY200906020), and the National Key Technology R&D Program (Grant No. 2007BAC03A01&2008-BAC40B02). The authors would like to give thanks to Prof. Q. Fu of Department of Atmospheric Science, University of Washington and Mr. X. W. Jing of NCC/CMA for his helps to the text of this paper.

## References

Ackerman AS et al (2000) Reduction of tropical cloudiness by soot. Science 288:1042–1047

Albrecht B (1989) Aerosols, cloud microphysics, and fractional cloudiness. Science 245:1227–1230

Allen RJ, Sherwood SC (2010) Aerosol-cloud semi-direct effect and land-sea temperature contrast in a GCM. Geophys Res Lett 37. doi:10.1029/2010GL042759

Ayash (2007) Development of an interactive model for studying aerosol-climate interactions using the Canadian aerosol module-Canadian climate center general circulation model modeling framework. Ph D Thesis, p 207

Bauer SE, Menon S, Koch D et al (2010) A global modeling study on carbonaceous aerosol microphysical characteristics and radiative effects. Atmos Chem Phys 10:7439–7456

Bellouin N, Jones A, Haywood J, Christopher SA (2008) Updated estimate of aerosol direct radiative forcing from satellite observations and comparison against the Hadley Centre climate model. J Geophys Res 113. doi:10.1029/2007JD009385

Binkowski FS, Shankar U (1995) The Regional Particulate Matter Model 1. Model description and preliminary results. J Geophys Res 100:26191–26209

Bond T, Bergstrom R (2006) Light absorption by carbonaceous particles: an investigative review. Aerosol Sci Technol 40:27–67

Bond T, Streets D, Yarber K, Nelson S, Wo JH, Klimont Z (2004) A technology-based global inventory of black and organic carbon emissions from combustion. J Geophys Res 109. doi:10.1029/2003JD003697

Brasseur GP, Hauglustaine DA, Walters S, Rasch PJ, Muller JF, Granier C, Tie XX (1998) MOZART, a global chemical transport model for ozone and related chemical tracers 1. Model description. J Geophys Res 103:28265–28289

Briegleb BP (1992) Delta-Eddington approximation for solar radiation in the NCAR Community Climate Model. J Geophys Res 97:7603–7612

Chung C, Ramanathan V (2006) Weakening of North Indian SST Gradients and the Monsoon Rainfall in India and the Sahel. J Climate 19:2036–2045

Chung SH, Seinfeld JH (2002) Global distribution and climate forcing of carbonaceous aerosols. J Geophys Res 107. doi:10.1029/2001JD001397

Cofala J, Amann M, Klimont Z, Schopp W (2005) Scenarios of world anthropogenic emissions of $SO_2$, NOx, and CO up to 2030, internal report of the transboundary air pollution programme, international institute for applied systems analysis. Laxenburg, Austria, p 17

D'Almeida GA, Koepke P, Shettle EP (1991) Atmospheric aerosols: global climatology and radiative characteristics. A. Deepak Publishing, Virginia, p 561

Dentener F, Kinne S, Bond T et al (2006) Emissions of primary aerosol and precursor gases in the years 2000 and 1750 prescribed datasets for AeroCom. Atmos Chem Phys 6:4321–4344

Easter RC (2004) MIRAGE: model description and evaluation of aerosols and trace gases. J Geophys Res 109. doi:10.1029/2004JD004571

Flanner MG, Zender CS, Randerson JT, Rasch PJ (2007) Present-day climate forcing and response from lack carbon in snow. J Geophys Res 112. doi:10.1029/2006JD008003

Ghan SJ, Easter RC, Chapman EG, Abdul-Razzak H, Zhang Y, Leung LR, Laulainen NS, Saylor RD, Zaveri RA (2001) A physically based estimate of radiative forcing by anthropogenic sulfate aerosol. J Geophys Res 106:5279–5293

Gong SL, Barrie LA, Blanchet JP (1997) Modeling sea-salt aerosols in the atmosphere 1. Model development. J Geophys Res 102:3805–3818

Gong SL, Barrie LA, Lazare M (2002) Canadian aerosol module: a size-segregated simulation of atmospheric aerosol processes for climate and air quality models 2. Global sea-salt aerosol and its budgets. J Geophys Res 107. doi:10.1029/2001JD002004

Gong SL et al (2003) Canadian aerosol module: a size-segregated simulation of atmospheric aerosol processes for climate and air

quality models 1. Module development. J Geophys Res 108. doi:10.1029/2001JD002002
Grini A, Myhre G, Sundet JK, Isaksen ISA (2002) Modeling the annual cycle of sea salt in the global 3D model Oslo CTM2: concentrations, fluxes, and radiative impact. J Climate 15:1717–1730
Gu Y, Liou KN, Xue Y, Mechoso CR, Li W, Luo Y (2006) Climatic effects of different aerosol types in China simulated by the UCLA general circulation model. J Geophys Res 111. doi:10.1029/2005JD006312
Hack JJ (1994) Parameterization of moist convection in the NCAR community climate model, CCM2. J Geophys Res 99:5551–5568
Hack JJ, Boville BA, Briegleb BP, Kiehl JT, Rasch PJ, Williamson DL (1993) Description of the NCAR community climate model (CCM2). Technical Report NCAR/TN-382 + STR, National Center for Atmospheric Research, p 120
Hansen J, Nazarenko L (2004) Soot climate forcing via snow and ice albedos. Proc Natl Acad Sci 101:423–428
Hansen J et al (1984) Climate sensitivity: analysis of feedback mechanisms, in climate processes and climate sensitivity. Geophys Monogr Ser 29:130–163
Hansen J, Sato M, Ruedy R (1997) Radiative forcing and climate response. J Geophys Res 102:6831–6864
Hansen J et al (2002) Climate forcings in Goddard Institute for Space Studies SI2000 simulations. J Geophys Res 107(D18). doi:10.1029/2001JD001143
Hansen J et al (2005) Efficacy of climate forcings. J Geophys Res 110. doi:10.1029/2005JD005776
Hauglustaine DA, Brasseur GP, Walters S, Rasch PJ, Muller J-F, Emmons LK, Carroll MA (1998) MOZART, a global chemical transport model for ozone and related chemical tracers 2. Model results and evaluation. J Geophys Res 103:28291–28335
Haywood JM, Ramaswamy V (1998) Global sensitivity studies of the direct radiative forcing due to anthropogenic sulfate and black carbon aerosols. J Geophys Res 103:6043–6058
Houghton JT, Meira Filho LG, Callander BA, Harris N, Kattenberg A, Maskell K (1996) Climate change 1995: the science of climate change. Cambridge University Press, Cambridge, p 572
IPCC (2007) Climate change 2007: the physical science basis. In: Solomon S, Qin D, Manning M, Chen Z, Marquis M, Averyt KB, Tignor M, Miller HL (eds) Contribution of working group I to the fourth assessment report of the intergovernmental panel on climate Change. Cambridge University Press, Cambridge, pp 131–217
Jacobson MZ (1997) Development and application of a new air pollution modeling system, part II, aerosol module structure and design. Atmos Environ 31:131–144
Jacobson MZ (2004) Climate response of fossil fuel and biofuel soot, accounting for soot's feedback to snow and sea ice albedo and emissivity. J Geophys Res 109. doi:10.1029/2004JD004945
Ji ZM et al (2011) Simulation of the anthropogenic aerosols over South Asia and their effects on Indian summer monsoon. Clim Dyn. doi:10.1007/s00382-010-0982-0
Kettle AJ, Andreae MO (2000) Flux of dimethylsulfide from the oceans: a comparison of updated data sets and flux models. J Geophys Res 105:26793–26808
Kiehl JT, Hack JJ, Bonan GB, Boville BB, Williamson DL, Rasch PJ (1998) The national center for atmospheric research community climate model: CCM3. J Climate 11:1131–1149
Kinne S et al (2006) An AeroCom initial assessment optical properties in aerosol component modules of global models. Atmos Chem Phys 6:1815–1834
Koch D (2001) Transport and direct radiative forcing of carbonaceous and sulfate aerosols in the GISS GCM. J Geophys Res 106:20311–20332
Koch D, Menon S, Genio AD (2009) Distinguishing aerosol impacts on climate over the past century. J Climate 22:2659–2677
Kristjansson JE, Iversen T, Kirkevag A, Seland Ø, Debernard J (2005) Response of the climate system to aerosol direct and indirect forcing: role of cloud feedbacks. J Geophys Res 110. doi:10.1029/2005JD006299
Kuhlmann J, Quaas J (2010) How can aerosols affect the Asian summer monsoon? Assessment during three consecutive pre-monsoon seasons from CALIPSO satellite data. Atmos Chem Phys 10:4887–4926
Lau KM, Kim KM (2006) Observational relationships between aerosol and Asian monsoon rainfall, and circulation. Geophys Res Lett 33. doi:10.1029/2006GL027546
Lau KM et al (2006) Asian summer monsoon anomalies induced by aerosol direct forcing: the role of the Tibetan Plateau. Clim Dyn 26:855–864. doi:10.1007/s00382-006-0114-z
Lestari R, Iwasaki T (2006) A GCM study on the roles of the seasonal marches of the SST and land-sea thermal contrast in the onset of the Asian summer monsoon. J Meteorol Soc Jpn 84(1):69–83
Li Z, Lee KH, Wang Y, Xin J, Hao WM (2010) First Observation-based Estimates of Cloud-free Aerosol Radiative Forcing across China. J Geophys Res 115. doi:10.1029/2009JD013306
Liao H, Seinfeld JH, Adams PJ, Mickley LJ (2004) Global radiative forcing of coupled tropospheric ozone and aerosols in a unified general circulation model. J Geophys Res 109. doi:10.1029/2003JD004456
Liou KN (2004) Introduction to atmospheric radiation version 2. China Meteorological Press, p 614
Liu Y, Sun J, Yang B (2009) The effects of black carbon and sulfate aerosols in China regions on East Asia monsoons. Tellus(B) 61:642–656
Lohmann U, Feichter J (2005) Global indirect aerosol effects: a review. Atmos Chem Phys 5:715–737
Marticorena B, Bergametti G (1995) Modeling the atmospheric dust cycle. 1: design of a soil-derived dust emission scheme. J Geophys Res 100:16415–16430
Meng Z, Dabdub D, Seinfeld JH (1998) Size-resolved and chemically resolved model of atmospheric aerosol dynamics. J Geophys Res 103:3419–3435
Menon S, Hansen J, Nazarenko L, Luo YF (2002) Climate effects of black carbon aerosols in China and India. Science 297:2250–2253
Ming Y, Ramaswamy V (2009) Nonlinear climate and hydrological responses to aerosol effects. J Climate 22:1329–1339
Myhre G (2009) Consistency between satellite-derived and modeled estimates of the direct aerosol effect. Science 325:187–190
Nakajima T, Yoon S-C, Ramanathan V et al (2007) Overview of the atmospheric Brown Cloud East Asian regional experiment 2005 and a study of the aerosol direct radiative forcing in East Asia. J Geophys Res 112. doi:10.1029/2007JD009009
Nightingale P, Malin G, Law C, Watson A, Liss P, Liddicoat M, Boutin J, Upstill-Goddard RC (2000) In situ evaluation of airsea gas exchange parameterizations using novel conservative and volatile tracers. Glob Biogeochem Cycles 14:373–387
Olivier J, Berdowski J, Peters J, Bakker J, Visschedijk A, Bloos J (2002) Applications of EDGAR including a description of EDGAR V3.0: reference database with trend data for 1970–1995. NRP Report, 410200 051. RIVM, Bilthoven
Pitari G, Mancini E, Rizi V, Shindell DT (2002) Impact of future climate and emissions changes on stratospheric aerosols and ozone. J Atmos Sci 59:414–440
Posselt R, Lohmann U (2009) Sensitivity of the total anthropogenic aerosol effect to the treatment of rain in a global climate model. Geophys Res Lett 36. doi:10.1029/2008GL035796
Ramanathan V, Ramana MV, Roberts G, Kim D, Corrigan C, Chung C, Winker D (2007) Warming trends in Asia amplified by brown cloud solar absorption. Nature 448:575–578

Ramaswamy V et al (2001) Radiative forcing of climate change. In: Climate change 2001: the scientific basis. In: Houghton M et al (eds) Contribution of working group I to the third assessment report of the intergovernmental panel on climate change. Cambridge University Press, pp 349–416

Randles CA, Ramaswamy V (2008) Absorbing aerosols over Asia: a geophysical fluid dynamics laboratory general circulation model sensitivity study of model response to aerosol optical depth and aerosol absorption. J Geophys Res 113. doi:10.1029/2008JD010140

Rasch PJ, Kristjansson JE (1998) A comparison of the CCM3 model climate using diagnosed and predicted condensate parameterizations. J Climate 11:1587–1614

Reddy MS et al (2005) Estimates of global multicomponent aerosol optical depth and direct radiative perturbation in the Laboratoire de Meteorologie Dynamique general circulation model. J Geophys Res 110. doi:10.1029/2004JD004757

Schulz M et al (2006) Radiative forcing by aerosols as derived from the AeroCom present-day and pre-industrial simulations. Atmos Chem Phys 6:5225–5246

Schumacher C, Houze RA (2006) Stratiform precipitation production over sub-Saharan Africa and the tropical East Atlantic as observed by TRMM. Q J R Meteor Soc 132:2235–2255

Slingo JM (1987) The development and verification of a cloud prediction scheme for the ECMWF model. Quart J Roy Meteor Soc 113:899–927

Slingo A (1989) A GCM parameterization for the shortwave radiative properties of clouds. J Atmos Sci 46:1419–1427

Streets DG et al (2003) An inventory of gaseous and primary aerosol emissions in Asia in the year 2000. J Geophys Res 108. doi:10.1029/2002JD003093

Takemura T, Nozawa T, Emori S, Nakajima TY, Nakajima T (2005) Simulation of climate response to aerosol direct and indirect effects with aerosol transport-radiation model. J Geophys Res 110. doi:10.1029/2004JD005029

Textor C et al (2006) Analysis and quantification of the diversities of aerosol life cycles within AeroCom. Atmos Chem Phys 6:1777–1813

Twomey SA (1977) The influence of pollution on the shortwave albedo of clouds. J Atmos Sci 34:1149–1152

Van der Werf GR, Randerson JT, Collatz GJ, Giglio L, Kasibhatla PS, Arellano AF, Olsen SC, Kasischke ES (2004) Continental-scale partitioning of fire emissions during the 1997 to 2001 El Nino/La Nina period. Science 303:73–76

Wang ZL, Guo PW, Zhang H (2009a) A numerical study of direct radiative forcing due to black carbon and its effects on the summer precipitation in China. Clim Environ Res 14:161–171 (in Chinese)

Wang ZL, Zhang H, Guo PW (2009b) Effects of black carbon aerosol in south Asia on Asian summer monsoon. Plat Meteorol 28:419–424 (in Chinese)

Warren S, Wiscombe W (1980) A model for the spectral albedo of snow. II: snow containing atmospheric aerosols. J Atmos Sci 37:2734–2745

Wilcox EM, Roberts G, Ramanathan V (2006) Influence of aerosols on the shortwave cloud radiative forcing from North Pacific oceanic clouds: results from the Cloud Indirect Forcing Experiment (CIFEX). Geophys Res Lett 33. doi:10.1029/2006GL027150

Wiscombe WJ (1980) Improved mie scattering algorithms. Appl Opt 19:1505–1509

Wu T, Wu G (2004) An empirical formula to compute snow cover fraction in GCMs. Adv Atmos Sci 21:529–535

Wu T, Yu R, Zhang F (2008) A modified dynamic framework for the atmospheric spectral model and its application. J Atmos Sci 65:2235–2253

Wu TW et al (2010) The Beijing Climate Center atmospheric general circulation model: description and its performance for the present-day. Climate Dyn 34:123–147. doi:10.1007/s00382-008-0487-2

Yan H (1987) Design of a nested fine-mesh model over the complex topograph, Part two: parameterization of the subgrid physical processes. Plat Meteorol 6(suppl):64–139

Zhang XY (2007) Aerosol over China and their climate effects. Adv Earth Sci 22(1):12–16

Zhang GJ, Mu M (2005) Effects of modifications to the Zhang-McFarlane convection parameterization on the simulation of the tropical precipitation in the National Center for Atmospheric Research Community Climate Model, version 3. J Geophys Res 110. doi:10.1029/2004JD005617

Zhang M, Lin W, Bretherton CS, Hack JJ, Rasch PJ (2003) A modified formulation of fractional stratiform condensation rate in the NCAR community atmospheric model CAM2. J Geophys Res 108. doi:10.1029/2002JD002523

Zhang X, Wang X, Yan P (2008) Re-evaluating the impacts of human activity and environmental change on desertification in the Minqin Oasis, China. Environ Geol 55:705–715

Zhang H, Wang ZL, Guo PW et al (2009) A modeling study of the effects of direct radiative forcing due to carbonaceous aerosol on the climate in East Asia. Adv Atmos Sci 26:57–66